Implications of non-ideal gas dispersion for underground hydrogen storage

Nazari, Farzaneh; Farajzadeh, Rouhi; Shokri, Javad; Vahabzadeh, Ehsan; Lopez-Porfiri, Pablo; Perez-Page, Maria; Niasar, Vahid

DOI
10.1016/j.cej.2025.160143

Publication date
2025

Document Version
Final published version

Published in
Chemical Engineering Journal

Chemical Engineering Journal 507 (2025) 160143

Contents lists available at ScienceDirect

Chemical Engineering Journal

journal homepage: www.elsevier.com/locate/cej

Implications of non-ideal gas dispersion for underground hydrogen storage

Farzaneh Nazari [a], Rouhi Farajzadeh [b,c], Javad Shokri [a], Ehsan Vahabzadeh [a], Pablo Lopez-Porfiri [a], Maria Perez-Page [a], Vahid Niasar [a,*]

[a] Department of Chemical Engineering, The University of Manchester, Oxford Road, Manchester, M13 9PL, UK
[b] Faculty of Civil Engineering and Geosciences, Delft University of Technology, P.O. Box 5048, Delft, GA 2600, The Netherlands
[c] Shell Global Solutions International B.V., The Hague, The Netherlands

ARTICLE INFO

Keywords:
Gas displacement
Dispersivity
Advection–dispersion
Numerical simulation

ABSTRACT

The gas displacement in porous media is a crucial process with extensive industrial and environmental applications. A notable example is underground hydrogen storage, where it is important to understand hydrogen mixing with cushion gas. The current paper explores anomalies in dispersion behaviour of gas mixtures under opposing flow directions (injection and production) from a modelling perspective. Due to the gaseous nature of the system, it presents significant complexities due to non-ideal mixing, compressibility, and higher diffusivity compared to Newtonian fluid transport. The findings reveal distinct dispersion behaviour during injection and production, where augmenting the mixture non-ideality enhanced the non-unique behaviour. In contrast to the dispersivity seen in Newtonian fluid flow in porous media, our research identifies that dispersivity in gas displacement depends not only on the porous medium but also on the gaseous components' properties.

1. Introduction

Dispersion in porous media is the spreading of a substance with time due to molecular diffusion and the spatial variability of velocity field [1,2]. The Advection–Dispersion Equation (ADE) is commonly used for studying the dispersion processes by applying a generalised dispersion coefficient [3–7]. The body of literature concerning solute transport and mixing in Newtonian liquid and aqueous phases is extensive and comprehensive [8–15]. Nevertheless, studies focusing on gas-phase dispersion in porous media are relatively limited in comparison. Gas phase dispersion in porous media has numerous industrial and environmental implications, such as carbon sequestration [16–18], enhanced gas recovery [19,20], natural gas storage [7,21–23], underground hydrogen storage (UHS) [24–27], transport in brain microcirculation [10], and food products [4,28].

Gas phase transport can exhibit differences from the liquid transport due to high compressibility and high diffusivity of gases [2]. Compressibility, in particular, can play an important role when a system undergoes significant pressure changes; for example, in the case of carbon capture and storage (CCS), pressurising the system until it reaches the CO_2 critical pressure leads to increased storage capacity due to gaseous supercritical properties, while a liquid CO_2 supercritical state acts in an opposite manner [22]. The diffusivity of gaseous molecules has also a direct relationship with their molecular weights, meaning small gas molecules (such as H_2) exhibit larger diffusion coefficients that can lead to a greater extent of spreading and loss, for instance concerning the UHS process [2].

Regarding UHS, there is still limited research in the literature on H_2 gas transport and H_2-cushion gas dispersive behaviour. Recently, few studies aimed at experimentally measuring the dispersion coefficients/dispersivity of these systems [24,29–31]. Kobeissi et al. [29] and Yang et al. [24] measured dispersion coefficients of binary H_2 - N_2/CH_4/CO_2 systems using the NMR technique. Their results indicate that no unique trend exists for the dispersion coefficient of these binary systems and the initial system pressure dictates the final dispersive behaviour. Thaysen et al. [30] also measured the dispersivity values for a H_2 - CH_4 binary system at varying pressure, temperature, and velocities, and found that the dispersive behaviour most weakly relies on the temperature as opposed to pressure of the system. Dabrowski [31] also investigated the dispersion coefficients of H_2 - CH_4 mixtures at varying low pressure, temperature, and velocities using a Raman spectrometer under opposing flow directions. Their results indicate dissimilar dispersion coefficients when using different invading components.

These studies, while offering preliminary insights into how the dispersive behaviour of a UHS system can depend on system properties, do not elucidate the mechanisms controlling the mixing in these binary systems. Additional modelling and experimental research is needed to fully understand the extent of mixing, dispersion, and the underlying causes of the observed dispersive behaviour in binary H_2-cushion gas

* Corresponding author.
E-mail address: vahid.niasar@manchester.ac.uk (V. Niasar).

https://doi.org/10.1016/j.cej.2025.160143
Received 9 August 2024; Received in revised form 22 December 2024; Accepted 31 January 2025
Available online 8 February 2025

systems. In the present study, our primary objective is to investigate the physics of miscible gas displacement in porous media assuming binary gas mixtures from a modelling perspective by addressing the following objectives within the framework of UHS, when H_2 mixes with cushion gases such as N_2, CH_4, and CO_2.

- To examine the differences and origin of dispersive behaviour of various binary gas mixtures in porous media.
- To study the influence of gas thermodynamic properties on the dispersion in porous media.
- To investigate the impact of flow direction (injection/production) on the dispersion in porous media.

2. Methodology

To accomplish the research objectives presented in the previous section, a single-phase, multi-component modelling study is conducted using the advection–dispersion equation [32]. The continuity equation for the fluid mixture is given by the following equation [33]:

$$\frac{\partial(\phi\xi)}{\partial t} = -\nabla\cdot(\xi\mathbf{v}) + q \tag{1}$$

, where, ϕ is rock porosity, ξ is the mixture molar density, and q represents the source/sink term. The mixture velocity, $\mathbf{v}$ is calculated using the Darcy's law [34] as demonstrated in Eq. (2) with μ, ρ, $\mathbf{k}$, and p being the fluid viscosity, mass density, permeability tensor, and pressure, respectively.

$$\mathbf{v} = -\frac{\mathbf{k}}{\mu}(\nabla p - \rho g \nabla z) \tag{2}$$

.

The fluid mixture is composed of multiple (here two) gas components with different concentrations. The conservation of mass of each component in a fluid mixture is given by Eq. (3) [33], where x_c is the mole fraction of the component c in the mixture (m), and $\mathbf{J}_c$ is also the dispersive mass flux that can be represented by Fick's law [35] ($\mathbf{J}_c = -\phi\xi\mathbf{D}_h\nabla x_c$) with $\mathbf{D}_h$ being the hydrodynamic dispersion coefficient in the tensorial form. The Stefan-Maxwell formulation [36] could also be employed to account for the dispersive/diffusive mass flux. However, since this study focuses on a binary gas system, Fick's law can sufficiently represent its diffusive/dispersive characteristics [37]. The hydrodynamic dispersion coefficient is the summation of effective diffusion coefficient, D_e, and mechanical dispersion, $\alpha|\mathbf{u}|$. The effective diffusion coefficient in porous media is known to be smaller than the molecular (binary) diffusion coefficient (D_m) due to the presence of solid obstacles and would be a function of porous media tortuosity and porosity [38,39]. In this study, the transversal dispersion has been ignored and only the longitudinal dispersion have been included, which reads ($D_{h_i} = \alpha u_i + D_e$), where u_i is the pore velocity in i direction and $D_e = \frac{\phi}{\tau}D_m$, with τ being the porous media tortuosity ($\tau = \phi^{-0.5}$ [38]).

$$\frac{\partial(\phi\xi x_c)}{\partial t} = -\nabla\cdot(\xi x_c\mathbf{v} + \mathbf{J}_c) + q_c \tag{3}$$

.

It is also known that D_m in gas mixtures is dependent on temperature, pressure, and concentration [40]. The low-pressure H_2 diffusion coefficient in binary gas systems was computed utilising the Wilke and Lee [41] relation (which is based on the Chapman–Enskog theory) [40]. However, this relation is only accurate for gases acting as ideal at low pressures. To tackle this, the Riazi and Whitson [42] correlation has been used to calculate the high-pressure diffusion coefficients as a function of binary mixture viscosity and density as can be seen in Eq. (4), where the 0 and + signs denote the low-pressure and high-pressure properties, respectively, and P_r and b and c are the reduced pressure and constants calculated based on the acentric factor, respectively [40,42]. The values of high-pressure diffusion coefficients for the four binary gas systems at P = 60 bar and T = 313 K are shown in Fig. 1.

$$\frac{(\xi D_m)^0}{(\xi D_m)^+} = 1.07\left(\frac{\mu^+}{\mu^0}\right)^{b+cP_r} \tag{4}$$

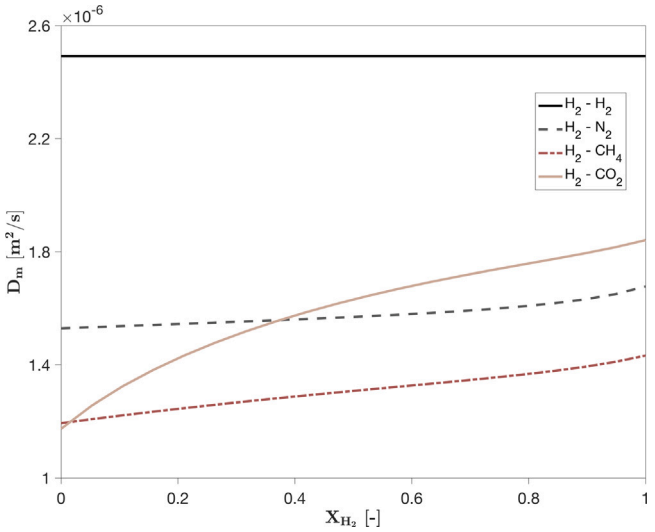

Fig. 1. The high-pressure diffusion coefficients for the four binary gas systems at P = 60 bar and T = 313 K calculated using Wilke and Lee [41] and Riazi and Whitson [42] (Eq. (4)) relations.

.

The pure and mixture gas properties, including the compressibility factors and compressibility values are calculated by Peng–Robinson [43] equation of state (PR EOS). A discussion on the choice of EOS for calculating the properties of H_2 containing mixtures and the comparison between PR [43], PC-SAFT [44], and Gerg 2008 [45,46] EOSs are presented in Appendix A (see Fig. A.1. Particularly for gaseous mixtures, care should be taken when defining the mixture molar density since it depends on the non-ideal properties of the gases, and it can have a significant impact on the miscible displacement process. Particularly, using ad-hoc assumptions (such as ideal gas mixture) makes it impossible to accurately reflect the true behaviour of the gases. In a real gas mixture, the molar densities are calculated based on Eq. (5), where Z_m, R, and T represent mixture compressibility factor, the universal gas constant and temperature, respectively. It is important to note that the compressibility factor and compressibility are distinct concepts. The compressibility factor (Z) corrects the volume of a gas to account for molecular interactions, such as attraction and repulsion, which deviate from the behaviour of an ideal gas where no such interactions occur. In contrast, compressibility ($c_p = \frac{1}{\xi}\frac{\partial\xi}{\partial P}$) describes how the volume of a gas changes in response to variations in pressure within the system. Pure component viscosities are also calculated using the correlation of Chung et al. [47] with the mixture viscosity computed by applying the Wilke [48] mixing rule.

$$\xi_m = \frac{P}{Z_m RT} \tag{5}$$

Eq. (1) is first solved to derive the velocity profile of fluid mixture, Eq. (3) can then be solved for $N_c - 1$ components in order to obtain the concentration profile. In this case, the PDEs are solved using a decoupled, finite volume, implicit method, and the transmissibilities are obtained using an upwinding scheme. Additionally, the average domain dispersion coefficient (D_h) is obtained by post-processing and fitting the effluent concentration data using the Ogata and Banks analytical solution [49] as demonstrated in Eq. (6), where C_0, C_i, and υ represent the concentration at the upstream boundary, initial concentration, and pore velocity, respectively.

$$C(x,t) = C_i + \frac{1}{2}(C_0 - C_i)\left[\mathrm{erfc}\left(\frac{x-\upsilon t}{2\sqrt{D_h t}}\right) + \exp\left(\frac{\upsilon x}{D_h}\right)\mathrm{erfc}\left(\frac{x+\upsilon t}{2\sqrt{D_h t}}\right)\right] \tag{6}$$

Table 1
A summary of basic parameters used in the model. The petrophysical properties and initial conditions are taken from Oldenburg [22].

Parameter	Value
Permeability, mD	1000
Porosity, (–)	0.30
Length, m	1.00
Initial Pressure, bar	60.00
Temperature, K	313.15
Water Diffusion Coefficient [50], m^2/s	10^{-9}
Longitudinal Dispersivity (Grid Size), m	0.005

3. Numerical modelling results

3.1. Model validation

An experimental investigation was carried out to test the validity of the numerical model, analytical solution, and to examine how the gas diffusion coefficient affects the dispersion coefficient of binary gases in porous media Appendix B. The experiments were conducted at low pressure and temperature conditions, where the highest values for diffusion coefficients was expected. The further high-pressure experiments and the investigation of the non-ideal gas behaviour was not feasible due to the setup hardware/equipment limitations as it is further discussed in Appendix B. Table B.4 and Fig. B.5 yield the following conclusions: (i) fitted velocity values agree with experimental boundary conditions, confirming the suitability of the Ogata-Banks solution. This outcome is essential to ensure validity of post-processing of the simulation data in the further modelling analysis; (ii) the numerical model fits the experimental data to ensure the numerical accuracy of the model; and (iii) diffusion controls the flow of gas mixtures in both the tube and core plug for the experiments. This is an important outcome of the experiments as compared to the diffusion in liquids, diffusion in gases are much stronger and thus cannot be neglected in the numerical simulations of mixing of gases.

3.2. Input data and the numerical domain

Table 1 outlines a list of basic parameters used in the model. The primary simulation domain is a thin two-dimensional rectangular with a constant pressure boundary (equal to the pressure of the system) located at its right side, while injection/production happens at the left boundary with constant mass rate. The right side also acts as a zero-gradient concentration boundary during injection, whereas during production, its concentration is constant (equal to 1). The domain is considered to be fully homogeneous to focus solely on the impact of gas mixing properties on dispersive behaviour as heterogeneity and the correlation lengths strongly affects the transport properties [51–53] and spreading [54]. It has been shown that for the gas mixing process, the presence of connate water saturation results in increased dispersion coefficients [20,55,56]. However, in this study, the impact of water saturation has been disregarded.

The simulations are conducted assuming binary gas mixtures, where H_2 acts as the main injecting/producing component, and $N_2/CH_4/CO_2/H_2$ are used as resident gases. The simulations were repeated for various injecting/producing velocities covering a Péclet Number ($Pe = \upsilon_{in} L_c / D_e$) range of about 5-$10^5$, defined based on interstitial velocity at inlet ($\upsilon_{in} = v_{in}/\phi$), L_c as the domain's length, and the starting effective diffusion coefficient of each case. It should be mentioned that the Péclet Number vary between different binary cases as the binary diffusion coefficients are calculated based on the gas types, composition, pressure, and temperature. A grid convergence study was conducted with a range of 50–400 grids in x-direction for H_2 - CO_2 displacement at $Pe = 100$. From 50 to 200 grids, the relative $\tilde{D_h}$ error compared to the lowest-grid case fell by around 8%, and by increasing the number of grids over 200, the relative error only changed by around 2%. Therefore, the total number of grids in x-direction was set equal 200, which resulted in a grid size and input dispersivity value of 0.005 m in x direction. A simple schematic of the employed simulation domain and its corresponding boundary conditions is shown in Fig. 2.

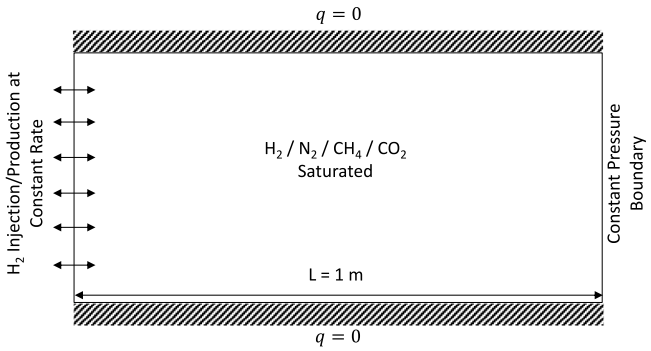

Fig. 2. The schematic of the simulation domain with initial and boundary conditions.

The Ogata and Banks [49] analytical solution was used to fit the numerically-derived effluent data against D_h and velocity, as shown by dashed lines in Fig. C.1. As illustrated in Fig. D.1, we have also used a method of moments approach based on step input [57] to calculate the dispersion coefficients in order to further validate the values obtained from the curve fitting. From the figure, it can be deducted that the values derived from the curve fitting of the analytical solution [49] are perfectly in line with the dispersion coefficient obtained from the moment method. Fig. 3 compares the effluent H_2 concentration as a function of dimensionless time, defined as the total injected pore volume divided to the total available pore volume in the domain, for different resident gases during H_2 injection and production. The effluent location is considered to be at the right and left boundaries during injection and production, respectively. According to this figure, at low velocities, $\upsilon \leq 1 \times 10^{-5}$ m/s (low Péclet numbers), the flow of H_2 mainly occurs due to diffusion as the advective force comes into play at larger time scales compared to the diffusive force and therefore, the gas flow happens as a result of diffusion only [58] following the binary diffusion coefficient trend of Fig. 1. Comparing various Péclet numbers, the distinction between different resident gases becomes more significant as one approaches larger Péclet numbers, at which point the flow properties are dictated by advective transport.

Dispersion for Newtonian fluid flow in porous media is introduced by $\tilde{D_h} = \alpha \upsilon^{\beta} + D_e$, in which α is the dispersivity which is a function of porous media properties, $\tilde{D_h}$ means macroscopic/upscaled dispersion coefficient, and β accounts for $\tilde{D_h} - \upsilon$ non-linearity and should be roughly equal 1 for Newtonian fluids. However, for gases, non-ideal gas mixing and compressibility control transport. Thus, we introduce a dispersivity correction factor related to the gas mixtures, $\delta = \frac{\alpha_g}{\alpha_w}$, which would read $\tilde{D_h} = \alpha_w \delta \upsilon^{\beta} + D_e$. Fig. 4 outlines the results of the upscaled dispersion coefficients ($\tilde{D_h}$) and correction factors (derived assuming $\beta = 1$) for all the studied cases. Fig. 4a, in particular, shows the plots of $\tilde{D_h}/D_0$ (D_0 is the equal to D_e at the start of injection/production) as a function of Péclet number for all the cases considered in this study. The H_2 and N_2 cases also exhibit comparable dispersion coefficients across various resident gases, with the scaled behaviour being quite similar to the water–water displacement. The disparity between the injection and production scenarios also rises when the resident gas is changed from H_2 to CO_2 ($H_2 \rightarrow N_2 \rightarrow CH_4 \rightarrow CO_2$). Fig. 4b also demonstrates the correction factor, δ, at various Péclet numbers for the different cases simulated in this study. From this figure, it can also be deducted that gas dispersivity is not comparable to that of water–water displacement and needs to be corrected for gas mixtures depending on their properties.

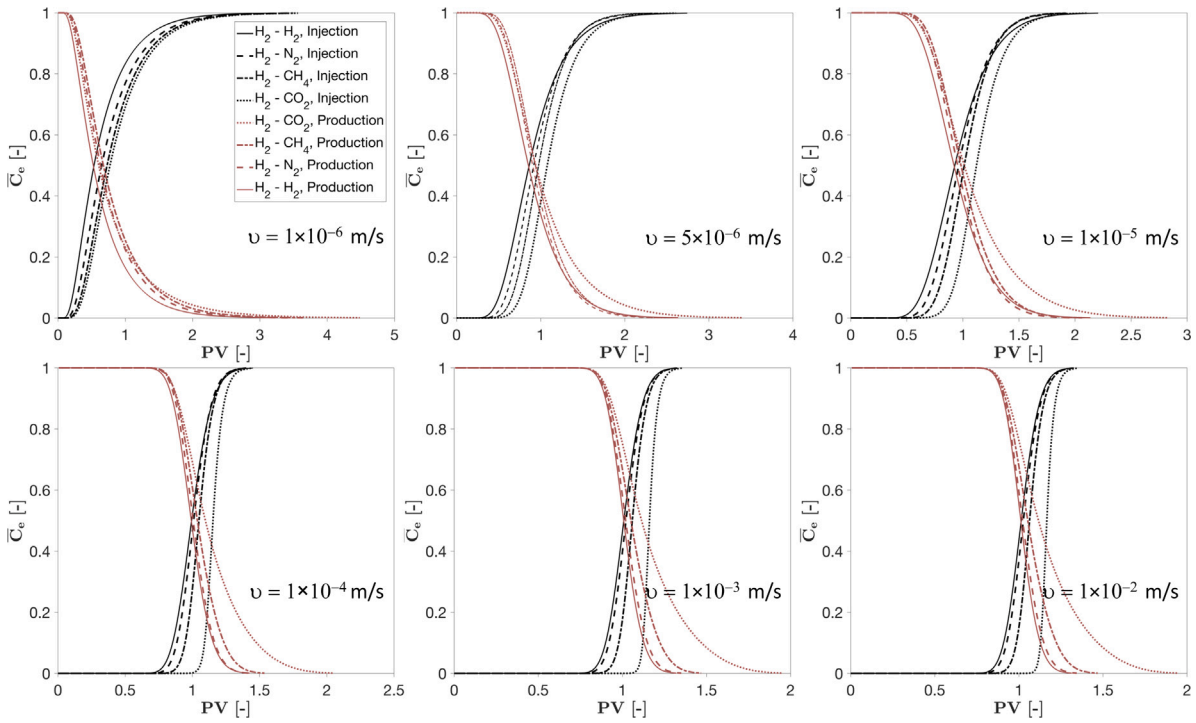

Fig. 3. Simulation results for effluent H_2 mole fractions as a function of time and injected pore volume for different residing gases during injection and production of H_2 at different ascending inlet/outlet velocities.

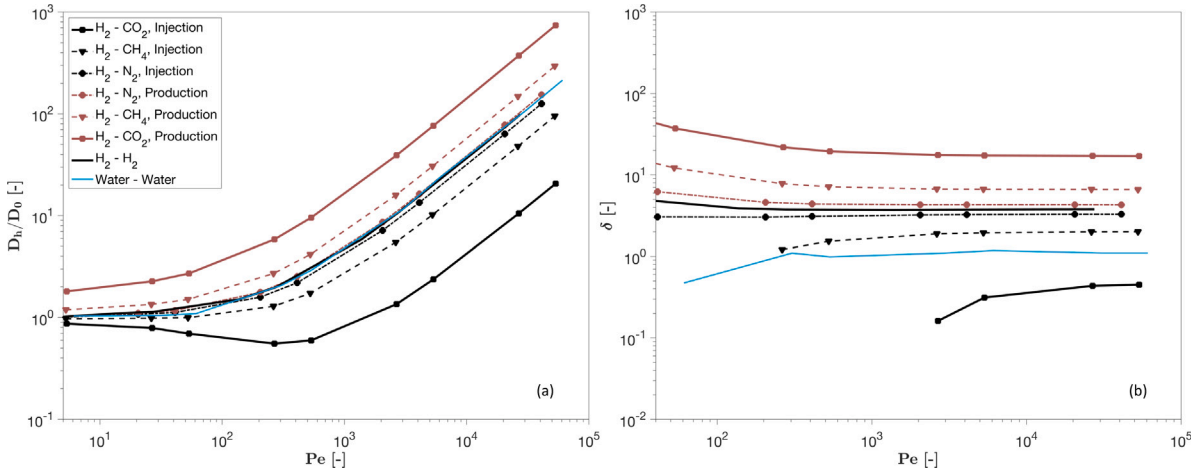

Fig. 4. (a) The longitudinal dispersion coefficient scaled by diffusion coefficient and (b) gas dispersivity correction factor (δ) as a function of Péclet number for different residing gases during injection and production. δ is calculated based on a water dispersivity value equal 0.003 m (section 3.4).

3.3. Origin of the non-unique dispersive behaviour

Comparing $\tilde{D}_h$ of different resident gases during H_2 injection, it can be deduced that $\tilde{D}_h$ decreases when changing the cushion gas from H_2 to CO_2 ($H_2 < N_2 < CH_4 < CO_2$), while the production scenarios follow an opposite trend. This dissimilar behaviour between injection/production processes have been discussed previously for liquid systems [59,60]. Dabrowski [31] also observed the non-unique dispersion coefficient between injection and production scenarios for H_2 - CH_4 displacement. Here, it was found that the non-ideal properties of gases mainly lies at the root of non-unique dispersion coefficients with the injection scenarios demonstrating a weaker dispersive behaviour. It should be mentioned that this dispersive behaviour cannot be solely interpreted in terms of H_2 spreading as a result viscosity difference between advancing and receding components, as N_2, CH_4, and CO_2 demonstrate similar viscosity values (around 1×10^{-5} Pa s) at the initial temperature/pressure conditions of this study, with N_2 having the highest viscosity amongst the resident gases. The impact of the viscosity ratio between the advancing and receding components has been investigated through additional simulations using the ideal gas mixture assumption for H_2 - N_2 and H_2 - CO_2 displacement as presented in Fig. 5. It was found that for the considered range of viscosity ratios, a homogeneous simulation domain, and low pressure changes within the considered system, a somehow unique injection/production dispersive behaviour exists.

It should also be noted that this behaviour cannot be investigated in terms of fluid compressibility either, since the range of applicable inlet/outlet mass rates used in the simulations prohibits any significant pressure changes within the system (below 0.5 bar). This can be explained in terms of mixing of real gases with different thermodynamic properties, here the gas compressibility factor, which account for the non-ideal behaviour of gases and determine how mixture (or pure)

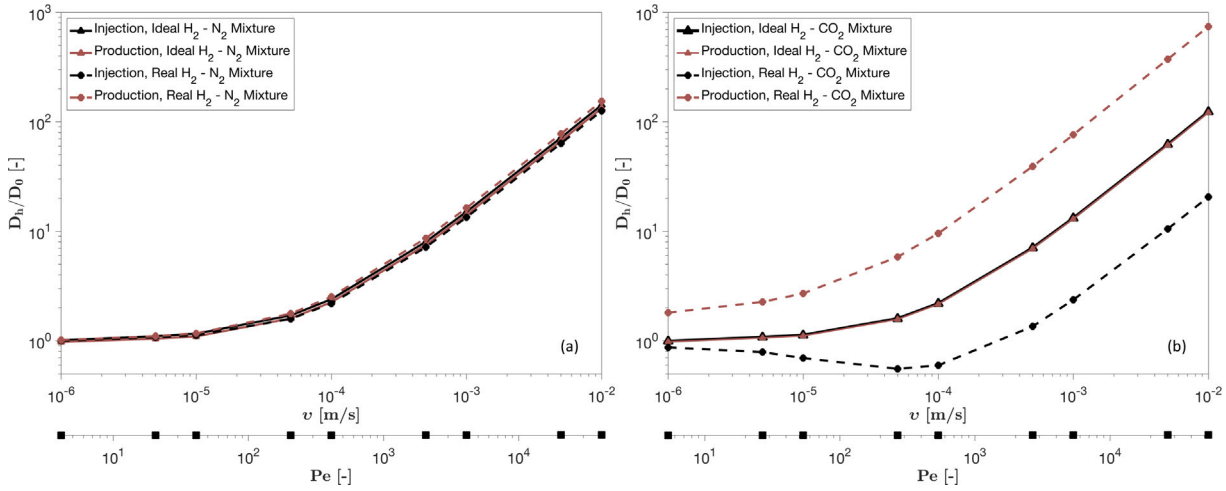

Fig. 5. The hydrodynamic dispersion coefficient, scaled by the diffusion coefficient, is plotted against the average domain pore velocity and Péclet number for (a) H_2 - N_2 and (b) H_2 - CO_2 displacements during H_2 injection and production. The figure compares the dispersion coefficient for ideal mixture assumptions (where the compressibility factor equals 1 for all gases) with those of real gas cases.

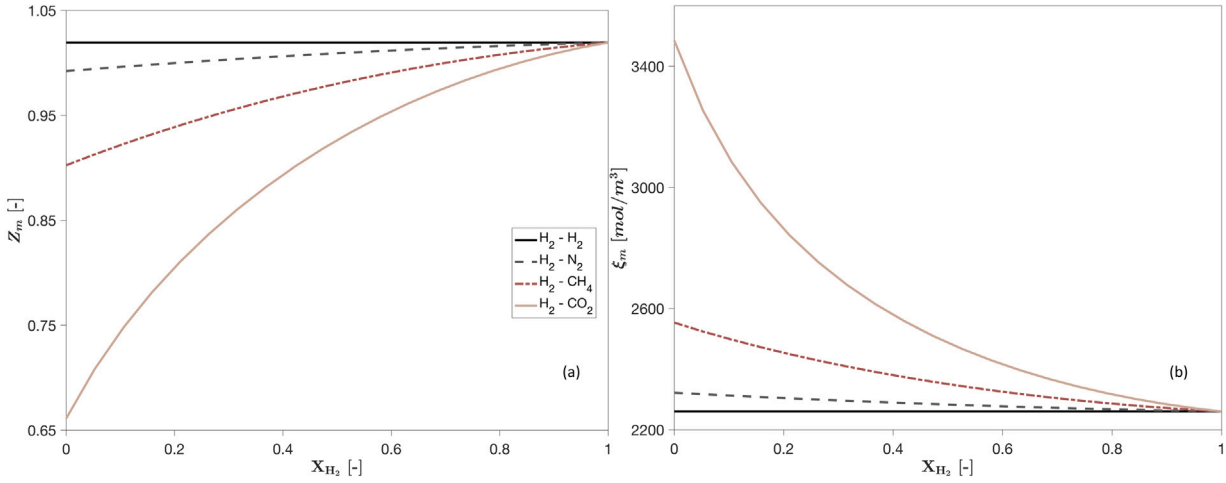

Fig. 6. (a) Mixture compressibility factor (derived from PR EOS [43]) and non-ideal mixture molar density (calculated according to Eq. (4)) as a function of H_2 mole fraction for different combination of binary gas mixtures.

molar densities (Eq. (5)) deviate from the ideal behaviour.

When the compressibility factor is considered, the molar density difference between the advancing and receding gases becomes more significant compared to ideal gas conditions, where gases exhibit identical molar densities ($\xi_c = \xi_m = \frac{P}{RT}$). This leads to the formation of a molar density gradient, driven by the gradient in the mixture's compressibility factor, which develops and evolves over the course of the simulation (Fig. 6a). Taking this molar density gradient into consideration, the introduction of H_2 results in a negative gradient ($\frac{\partial \xi_m}{\partial x} \geq 0$), while the removal of H_2 from the system causes the gradient to become positive ($\frac{\partial \xi_m}{\partial x} \leq 0$). As a result, the dispersion coefficients decrease during H_2 injection and increase during its production. Furthermore, among the cushion gases, CO_2 exhibits the largest variations in compressibility factor, following the order $Z_{CO_2} < Z_{CH_4} < Z_{N_2} < Z_{H_2}$. This indicates that the H_2-CO_2 mixture deviates the most from ideal gas behaviour and experiences the greatest molar density fluctuations compared to the other gas mixtures (see Fig. 6).

Here, we define a new term called the compressibility factor ratio between advancing and receding components ($Z_r = Z_{Adv}/Z_{Rec}$). During injection ($Z_r > 1$), the displacement front would behave more sharpely compared to the production cases ($Z_r < 1$). The H_2 - CO_2 mixture would also have the largest Z_r during injection, meaning the dispersive behaviour will become less significant as opposed to the production scenarios. Based on the simulation results (Fig. 7), an exponential relationship exists between the gas dispersivity correction factors and compressibility factor ratio at advection-dominated regimes. Therefore, a general correlation is proposed to relate the correction factor to Z_r at high Péclet numbers ($Pe > 100$), as demonstrated by Eq. (7) and Fig. 7.

$$\delta = 131.98 \exp(-4.88 Z_r) \quad ; \quad 0.6 \leq Z_r \leq 1.6 \tag{7}$$

The compressibility factors also present dependence on pressure and temperature of the system, with varying direction and magnitude for each component (see Fig. 8a). The figure shows the plot of compressibility factor of pure gas components at a temperature of 313.15 K. It is evident that when pressure rises, the compressibility factor of H_2 slightly increases, whereas that of CH_4 and CO_2 sharply decreases. The N_2 compressibility factor has likewise remained relatively consistent throughout the temperature and pressure range under consideration. This emphasises how important non-ideal properties of gas mixtures are, particularly for H_2 - CH_4 and H_2 - CO_2 displacement, and how a more enhanced non-unique injection/production behaviour can be expected at higher pressures (Fig. 8b).

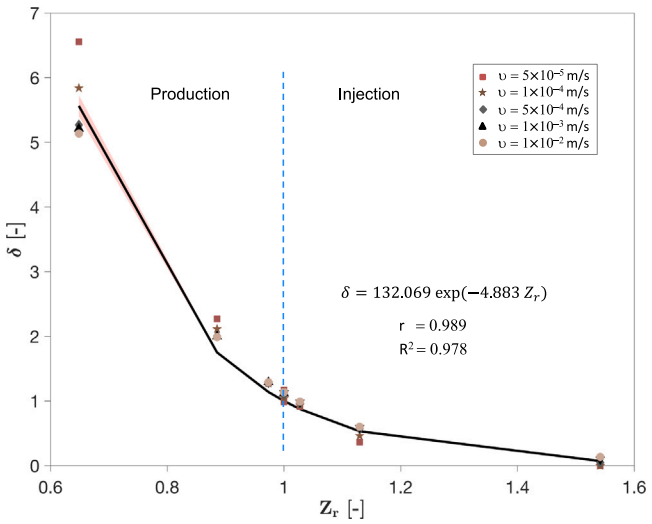

Fig. 7. Gas dispersivity correction factor (δ) versus compressibility factor ratio ($Z_r = Z_{Adv}/Z_{Rec}$) at different inlet/outlet pore velocities. The H_2 injection and production cases are denoted by $Z_r > 1$ and $Z_r < 1$, respectively, with the H_2 - H_2 displacement represented by $Z_r = 1$. The production and injection of H_2 in the H_2 - CO_2 displacement are also shown by the lowest and highest Z_r. The continuous black line presents the fitted values generated using the correlation shown in Eq. (7). The values of correlation coefficient (r) and coefficient of determination (R^2) is shown on the graph.

Table 2
Fitted velocity exponent (β) and gas dispersivity correction factor (δ) based on the equation, $D_h = \alpha\delta u^{\beta} + D_e$, for different gas mixtures during injection and production of H_2. The fitted dispersivity value and velocity exponent for water–water displacement is equal 0.003 m and 0.991, respectively.

	Injection, β	Production, β	Injection, δ	Production, δ
H_2 - H_2	1.003	1.003	3.872	3.853
H_2 - N_2	1.002	0.997	3.349	4.244
H_2 - CH_4	1.008	0.996	2.114	6.476
H_2 - CO_2	1.102	0.992	0.831	16.351
H_2 - N_2, Ideal Gas	1.001	0.999	3.832	3.759
H_2 - CO_2, Ideal Gas	1.002	0.999	3.848	3.774

3.4. Nonlinear behaviour of dispersion coefficient

It has been argued that the dispersion coefficient does not always exhibit a linear relationship with velocity and the degree of this non-linearity depends on the porous media and fluid properties. This study also investigates the dispersion coefficient-velocity non-linear behaviour by introducing the exponent β. δ (correction factor) and β values have been used to fit $\tilde{D}_h$ employing the equation $\tilde{D}_h = \alpha\delta u^{\beta} + D_e$ [61]. Table 2 shows the values of the these two fitting parameters for the majority of the simulation cases of this study. The fitting process for water–water displacements leads to β and δ values equal 0.991 and 0.003 m, respectively. The correction factors for gas mixtures are also derived based on this value of dispersivity for water. From the table, the following can be deduced: (i) The H_2-H_2, H_2-N_2, and ideal gas cases exhibit relatively consistent dispersivity values, while the H_2-CO_2 and H_2-CH_4 cases show significant deviations, with production leading to much higher dispersivities. (ii) The nonlinearity between dispersion coefficients and system velocities is minimal for the H_2-H_2, H_2-N_2, and ideal gas cases, but becomes more pronounced when CH_4 and CO_2 are the resident gases. These nonlinear behaviours and variations in dispersivity align with previous observations regarding gas non-ideality, as reflected in the compressibility factors.

4. Conclusions

The present study examined the dispersive properties of binary gas systems within porous media, specifically focusing on UHS. A numerical model, able to consider the non-ideal behaviour and compressible nature of gases, was developed and employed to analyse binary gas displacement. The comprehensive model and the application of the analytical Ogata-Banks solution were validated through a proposed experimental procedure. However, the further use of the experimental setup was discontinued due to its limitations and a lack of resources.

In summary, it was discovered that different binary gas combinations can behave differently in a displacement process. Increasing the non-ideality of the gas mixture (enhanced compressibility factor difference between the components) resulted in enhanced dispersion characteristics, mixing and boosted difference between injection/production scenarios when comparing different binary gas mixtures. A correction factor for dispersivity was introduced, which was found to vary depending on the binary mixture used, indicating the influence of fluid characteristics rather than porous medium physical properties.

In the context of UHS operations, while CO_2 exhibited less mixing with H_2 under advective regimes and during injections, the production phase showed significantly higher dispersion characteristics. This makes CO_2 a less favourable option for use in such systems. It should be noted that this study did not take into account the situations where CO_2 will act as a supercritical fluid, in which case, the dispersive behaviour can be significantly impacted by high viscosity and density variations [22]. It should also be noted that CO_2 may be a less efficient cushion gas as it enhances the methanogenesis and microbial activities to consume hydrogen which is out the scope of this study.

Additionally, the effects of diffusion coefficient on the dispersive behaviour of gases were examined from modelling and experimental standpoints. The transport properties of gases are majorly controlled by diffusion in a wide array of applicable Péclet numbers, and therefore, diffusion time scales are important in determining the H_2 purity and loss. This behaviour will continue to be enhanced, particularly during shut-in periods and far-well regions where the H_2 flow solely occurs as a result of diffusion [58].

It is important to note that the overall efficiency of the operation is influenced by the interaction of various additional factors, such as the effects of gravity, heterogeneity, and compressibility (if applicable). These factors, along with a more in-depth investigation into the effects of heterogeneity, should be considered in future research.

CRediT authorship contribution statement

Farzaneh Nazari: Writing – review & editing, Writing – original draft, Visualization, Validation, Software, Methodology, Investigation, Formal analysis, Data curation, Conceptualization. **Rouhi Farajzadeh:** Writing – review & editing, Validation, Supervision, Methodology, Conceptualization. **Javad Shokri:** Writing – review & editing, Validation, Data curation. **Ehsan Vahabzadeh:** Writing – review & editing, Validation, Formal analysis. **Pablo Lopez-Porfiri:** Resources, Formal analysis. **Maria Perez-Page:** Resources, Formal analysis. **Vahid Niasar:** Writing – review & editing, Supervision, Resources, Methodology, Funding acquisition, Formal analysis, Conceptualization.

Declaration of competing interest

The authors declare that they have no known competing financial interests or personal relationships that could have appeared to influence the work reported in this paper.

Acknowledgements

Rouhi Farajzadeh thanks Shell Global Solutions International B.V. for granting permission to publish this paper. The Presidential Doctoral Scholarship of the University of Manchester funded the FN's PhD study. VN and JS's time was supported by EPSRC EP/W008718/1 award.

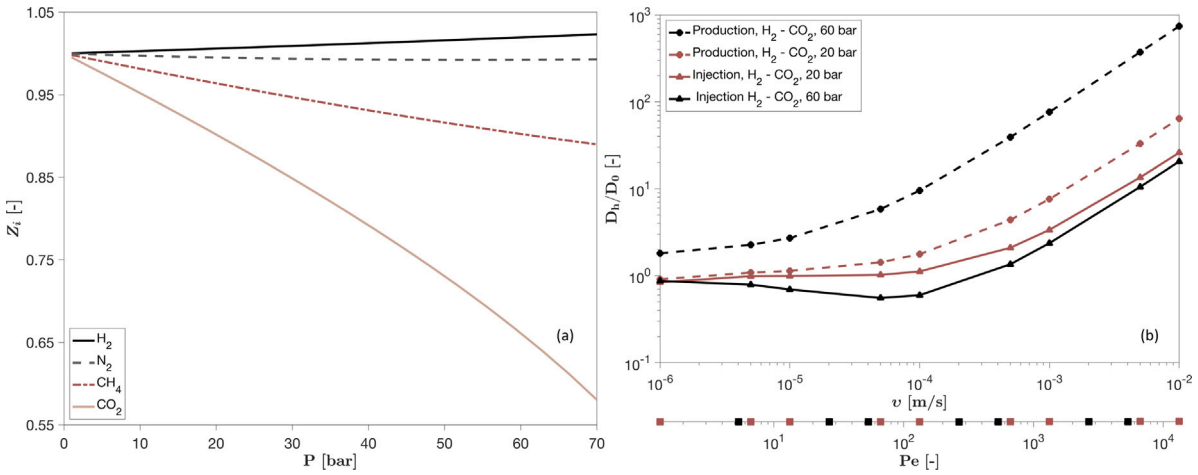

Fig. 8. (a) Impact of pressure on pure gas compressibility factors at a temperature equal 313.15 K, and (b) Upscaled dispersion coefficients as a function of Péclet number at two different pressures equal 20 and 60 bar for H_2 - CO_2 displacement.

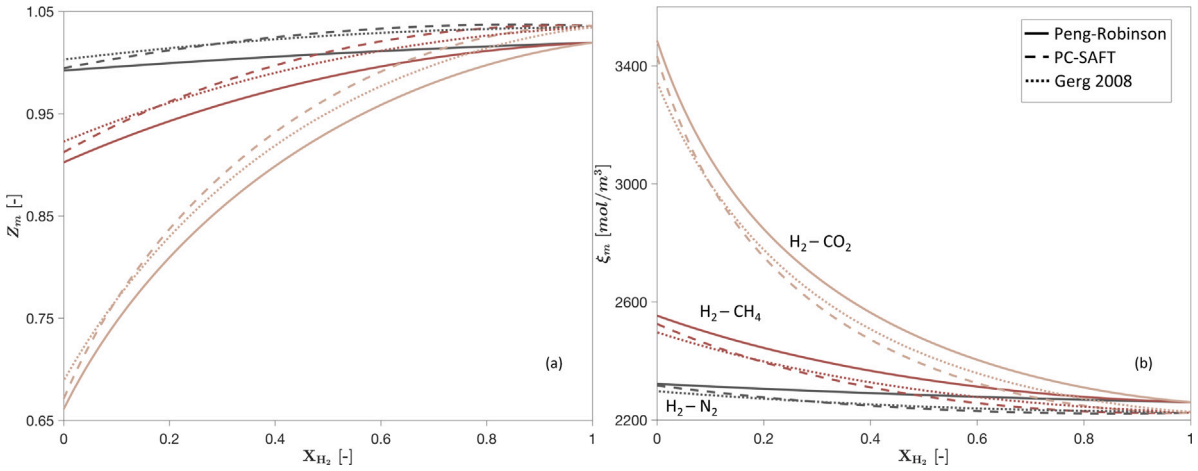

Fig. A.1. (a) Mixture compressibility factor and (b) mixture molar density calculated using three equations of states (PR [43], PC-SAFT [44], and Gerg 2008 [45,46]) as a function of hydrogen mole fraction in the binary mixture.

Appendix A. Equation of states

A.1. Comparison between equations of states

This section presents a comparison of the results of different equations of states, namely PR [43], PC-SAFT [44], and Gerg 2008 [45,46] EOSs (the reference EOS for H_2), in terms of compressibility factor and mixture molar density. It is widely known that conventional equations of states do not accurately predict the properties of H_2 containing mixtures, especially under very high pressure and low temperature conditions [62]. This is due to the unique properties of H_2, such as a low molar mass. In order to confirm the applicability and validity of PR EOS (used in this study), we have calculated the two main thermodynamic properties of our model (compressibility factor and mixture molar density) using the three-mentioned EOSs. It can be seen from Fig. A.1 that PR EOS slightly underestimates the Z factor of the H_2 containing mixtures leading to the slight overestimation of mixture molar densities when compared to Gerg 2008 and PC-SAFT EOSs. However, in our view, the observed difference does not justify the introduction of a more complex EOS into the model. It should also be mentioned that this study does not deal with cryogenic temperature conditions and thermal properties of H_2 (such as specific heat capacity) where the most deviations in H_2 properties are observed.

Appendix B. Model validation

B.1. Experimental setup and materials

A gas separation unit originally designed to evaluate the efficiency of membranes in separating gases [63,64] was modified and employed for studying the mixing of binary gases through a core plug, representing a subsurface porous medium. Fig. B.1 illustrates a schematic of the employed gas separation setup. The rig encompasses, (i) a micro gas chromatograph (GC) system (Agilent Micro GC, G3581 A) coupled with a TCD detector and an MS5 A HI column (Ar 99.998% as the carrier) used to analyse the composition of the effluent gas; (ii) a core holder containing a sandstone core plug with a length and diameter of 4.7 cm and 1.1 cm, respectively; (iii) a Mass Flow Controller (MFC) (Alicat Scientific MC Series) for each gas placed at the inlet for injection of gases, and one MFC on the outlet to control the rate of outflow gas; (iv) a three-way valve (V1) placed at the inlet to enable the flow from the MFCs to exhaust or to the core holder. To reduce gas mixing in the tubing, the length of the tube connected to the core holder (shown in red) was minimised. A hydrogen generator (Claind, Hggen 400), operating at a maximum pressure of 6 bar, supplied H_2 (99.9995%) for the experiments, whereas, CH_4 (99.9995%) and N_2 (99.998%) were acquired from BOC company.

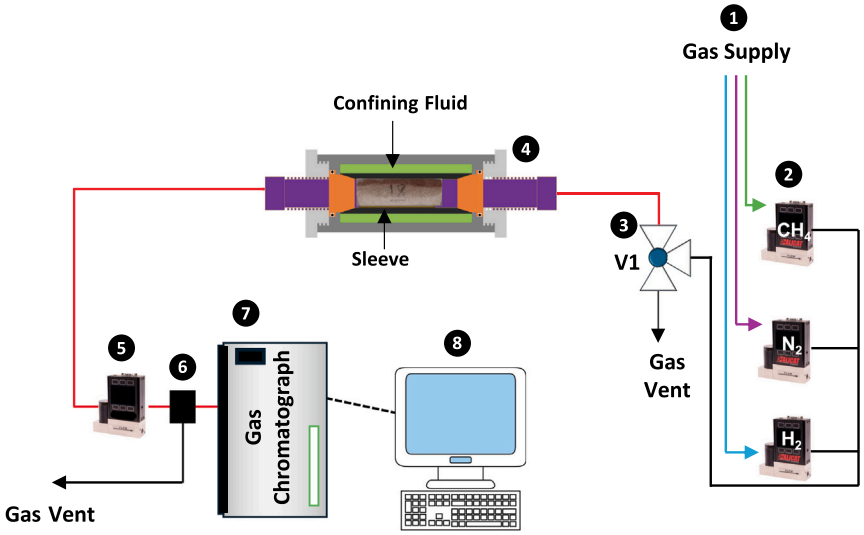

Fig. B.1. A schematic of the gas separation unit modified to study the mixing of binary gas systems in porous media. The setup includes (1) the gas supply unit; H_2 is provided through the H_2 generator, while N_2 and CH_4 are coming from gas cylinders, (2) inlet MFCs for injection of gases, (3) a three-way valve to direct flow to the vent or the sample, (4) a core holder containing the core plug, (5) outlet MFC, (6) auto-sampler, (7) gas chromatography, and (8) a computer setup to process the GC readings and controlling the MFCs.

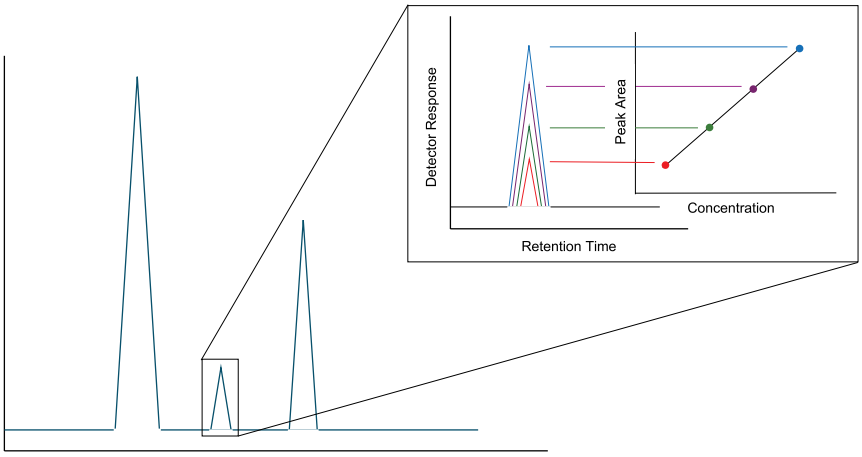

Fig. B.2. An illustration of the GC response and the linear calibration procedure. The figure is adapted from Agilent [65].

B.2. Gas chromatography

A GC analysis was used for the real-time analysis of the permeate composition. The components were identified according to the thermal conductivity; the higher the thermal conductivity, the quicker the component was detected by GC. Consequently, real-time results as a chromatogram, displaying the retention time - duration needed for each component to pass through the column and into the detector [65]- on the x-axis and the detector response on the y-axis (Fig. B.2), were generated. The retention time varies for each gas and depends on instrument conditions, such as type of column, pressure, and temperatures.

B.3. Calibration of gases

A calibration curve is required to relate the GC peak area to its corresponding gas concentration. It was performed by running standard mixtures at various concentrations and plotting the results against detector response as shown in the subset of Fig. B.2. For the calibration, the core plug (and the holder) was replaced with a bypass to fully allow the flow of gases. The calibration process was done separately for each binary gas mixture (H_2 - N_2 and H_2 - CH_4). To guarantee the repeatability of the GC peak areas, six different GC scans were carried out at each input concentration. The mean of the final four measured GC scans was utilised as the final peak area at each concentration. Fig. B.3 depicts the calibration results for H_2 - CH_4 and H_2 - N_2 systems.

B.4. Permeability measurements

The absolute permeability of the core plug was calculated using the Klinkenberg equation [66] (B.1), where K_g, K, and b represent gas permeability, absolute permeability, and the Klinkenberg coefficient. Gas permeabilities were calculated using Darcy's law [34] at 4 different flow rates. As it is shown in Fig. B.4, the absolute permeability of the core plug (K) was found to be around 34.24 mD, and b = 1.6 bar.

$$K_g = K\left(1 + \frac{b}{P}\right) \tag{B.1}$$

B.5. Gas-mixing experiments

The experiments were conducted at 22 °C using two binary gas mixtures, H_2 - N_2 and H_2 - CH_4. The core plug was initially saturated

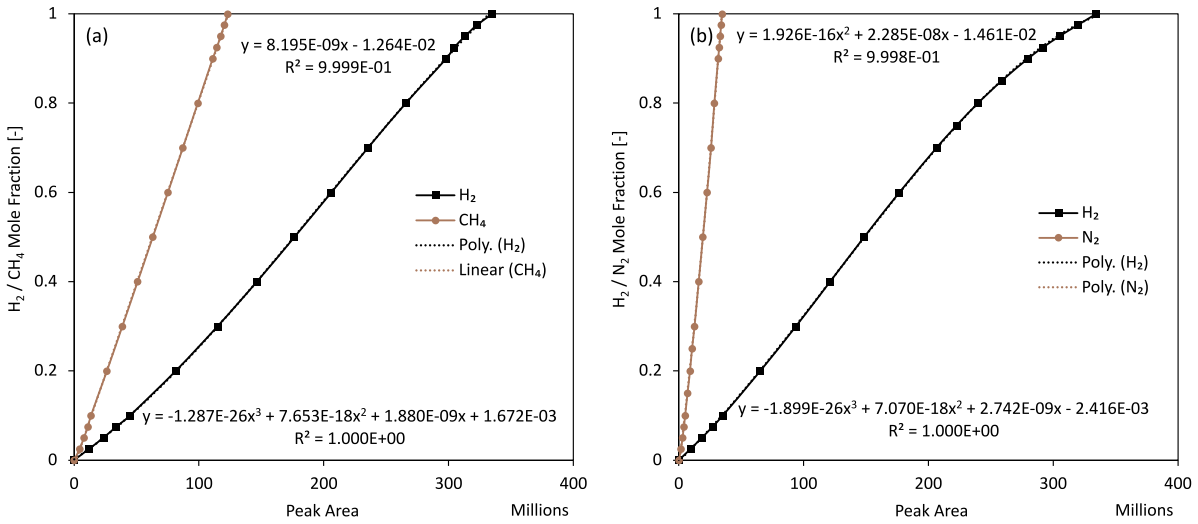

Fig. B.3. The calibration curves for (a) H_2 - N_2 and (b) H_2 - CH_4 showing the mole fraction of the outlet gas as a function of GC peak area.

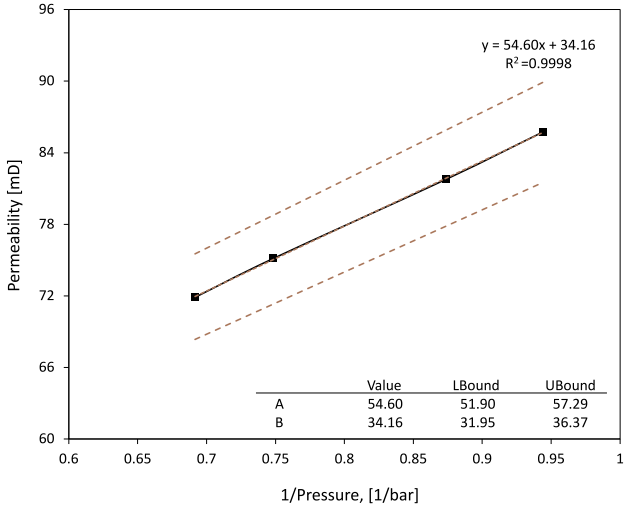

Fig. B.4. The Klinkenberg [66] plot -gas permeability versus inverse of mean pressure. The linear curve fitting data (y = Ax + B) and lower/upper prediction bounds are detailed in the figure as well.

with either N_2 or CH_4 at approximately 1.5 bar gauge, and swept by H_2 at 1 cc/min (at experimental conditions). The reverse process, involving the injection of CH_4/N_2 in an H_2-saturated domain, was halted due to technical issues, which will be elaborated on in the following sections. A confining pressure of 30 bar was applied to ensure the rubber sleeve was securely attached to the core plug's surroundings, ensuring that all the injected gas passed exclusively through the core plug and not around it. The overall procedure for conducting gas-mixing experiments through a core plug is as follows:

1. Saturate the core plug and connected tubing with N_2/CH_4 by injecting gases using MFCs. To ensure complete saturation, several GC scans were conducted.
2. Increasing the pore pressure to around 1.5 bar. Shutting the outlet and inlet MFCs off.
3. Switch the V1 valve to the vent position. Injecting H_2 with a high flow rate to replace N_2/CH_4 in the black tube down to the valve V1. Followed by increasing the pressure in the black line depicted in Fig. B.1 to around 1.5 bar.

Table B.3
Dispersion coefficient and velocity definitions.

D_1	Sum of dispersion coefficients in tubing and core plug, derived from fitting of experimental data.
u_1	Average velocity of the tubing and core plug, derived from fitting of experimental data.
D_2	Dispersion coefficient of the tubing, calculated from Taylor-Aris relation [67] (Eq. (B.3)).
D_3	Dispersion coefficient of the core plug, derived from Eq. (B.2).
u_2	Average core plug velocity, calculated from a parabolic velocity distribution with a maximum equal u_1.
D_4	Dispersion coefficient of the core plug, derived from fitting of simulated breakthrough curves.
u_3	Average core plug velocity, calculated from fitting of simulated breakthrough curves.

4. Switch the V1 valve, allowing H_2 to enter the core plug, simultaneously setting the MFCs in the inlet and the outlet to the desired flow rates, and start GC scans.
5. Employ the calibration data (Fig. B.3) to calculate the mole fractions of gases measured at the outlet of the core holder.

B.6. Analysing the experimental data

Fig. B.5 illustrates breakthrough curves (H_2 mole fraction as a function of experimental time) for H_2 - N_2 and H_2 - CH_4 systems. As mentioned earlier, H_2 was injected into a core plug saturated with N_2/CH_4. Each experiment was performed twice to ensure reproducibility of the results as shown in Fig. B.5a.

As Eq. (B.2) presents, the dispersion coefficient derived from the experiment could be due to the mixing of gases occurring in the core plug and tubing (coloured in red in Fig. B.1). The velocity and dispersion coefficient terms used in the remaining part of this section are listed in Table B.3. Steps below were followed to eliminate the effect of mixing in tubing, and derive the pure dispersion of the porous medium.

1. The average velocity and dispersion coefficient of the experiment (D_1 and u_1) were quantified by the inverse application of Ogata-Banks analytical solution [49] using the breakthrough data shown in Fig. B.5a. The curve fitting results are presented in Fig. B.5b.
2. As Eqs. (B.2) and (B.3) show, the dispersion coefficient of the core plug (D_3) was derived by subtracting the total experiment dispersion coefficient (D_1) from the tubing dispersion coefficient

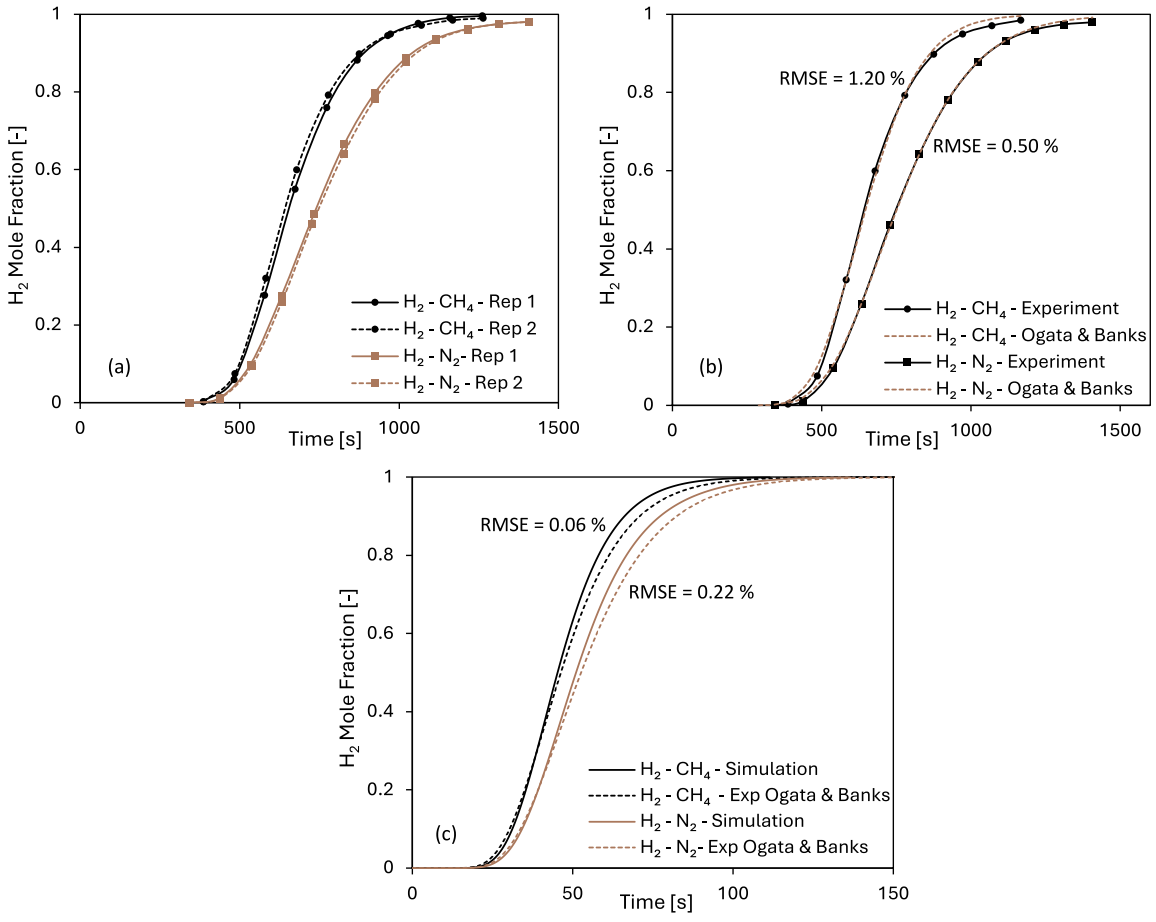

Fig. B.5. (a) The breakthrough curves for H_2 - N_2 and H_2 - CH_4 systems with H_2 as the advancing component. The generation of the breakthrough curves are done for two repetitions of the experimental procedure. (b) The experimentally-measured breakthrough curves along with the fitted Ogata-Banks [49] analytical solution. (c) The final breakthrough curves for the core plug. The data is based on the (1) forward application of Ogata-Banks solution from the experimental data (dashed lines) and (2) the numerical model depicted in the 'Methodology' section (continuous lines). The RMSE values show the fitting errors (root mean square error) of the concentration profiles.

(D_2, derived using Taylor-Aris formulation [67,68]). The binary diffusion coefficients (D_m) are also calculated using the Wilke and Lee correlation [41] separately for H_2 - N_2 and H_2 - CH_4 systems at $T = 297.15$ K and$P = 1.5$ bar.

$$D_1 = D_2 + D_3 \tag{B.2}$$

$$D_2 = D_m + \frac{r^2 u_1^2}{48 D_m} \tag{B.3}$$

3. A parabolic velocity profile was generated at the inlet of the core plug, with its maximum velocity, matching the fitted velocity from step 1 (u_1). The average of the parabolic velocity profile (u_2) was then used to derive the breakthrough curve of the core plug. The breakthrough curve of the core plug was regenerated by the forward application of the Ogata-Banks solution [49] using the core plug dispersion coefficient (D_3) and the mentioned average velocity (u_2) as inputs.
4. The numerical simulations were conducted using the same parabolic velocity profile (step 3) as its input. The numerical average domain velocity (u_3) and dispersion coefficient (D_4) were calculated by the fitting of Ogata-Banks solution [49]. It should be noted that the core plug simulations were conducted considering an effective diffusion coefficient definition, meaning $D_e = \frac{\phi}{\tau} D_m$, where τ represents the tortuosity of porous media ($\tau = \phi^{-0.5}$) [38,69,70]. The porosity of the core plug was 0.1. It should be mentioned that calculating tortuosity values based solely on the porosity of the porous media is flawed as it would yield equal tortuosity values for porous mediums having equal porosity but different porous structures. However, experimentally calculating the tortuosity of the porous medium is not a straightforward task to achieve. Moreover, the aforementioned correlation yields adequate results for this study's application.
5. The numerical simulation results were validated against the core plug breakthrough data of the experiments (steps 1–4), as shown in Fig. B.5c.

Table B.4 additionally displays the dispersion coefficients and final velocity values that were determined by the experiments (tubing + core plug), analytical solution (experimental core plug) and the numerical model (core plug). It can be deducted that the (i) fitted velocity values are in line with experimental boundary conditions endorsing the adequacy of the Ogata-Banks solution (1 cc/min injection results in a velocity equal (1.75×10^{-3} m/s) and ii) the numerical model combined with the Ogata-Banks analytical solution give accurate results when compared to the experimental data.

B.7. Discussion on the experimental challenges

The conducted experiments could not represent the actual flow conditions in an underground storage system and provide insights into the real-life differences between the gases due to limitations of the experimental apparatus and complications in performing the experiments as follows:

- Firstly, the pore pressure was limited and could not be elevated to represent an actual storage system due to the pressure rating

Table B.4
The values of dispersion coefficient and velocity for the total experimental length, core plug, and those derived from the numerical model. The indices are explained in Table B.3.

	Experiment: Tube + Core Plug		Experiment: Core Plug		Numerical: Core Plug	
Mixture	D_1, m^2/s	u_1, m/s	D_3, m^2/s	u_2, m/s	D_4, m^2/s	u_3, m/s
H_2 - CH_4	4.56×10^{-5}	1.64×10^{-3}	2.59×10^{-6}	9.60×10^{-4}	2.29×10^{-6}	9.94×10^{-4}
H_2 - N_2	5.45×10^{-5}	1.40×10^{-3}	2.52×10^{-6}	8.40×10^{-4}	2.16×10^{-6}	8.74×10^{-4}

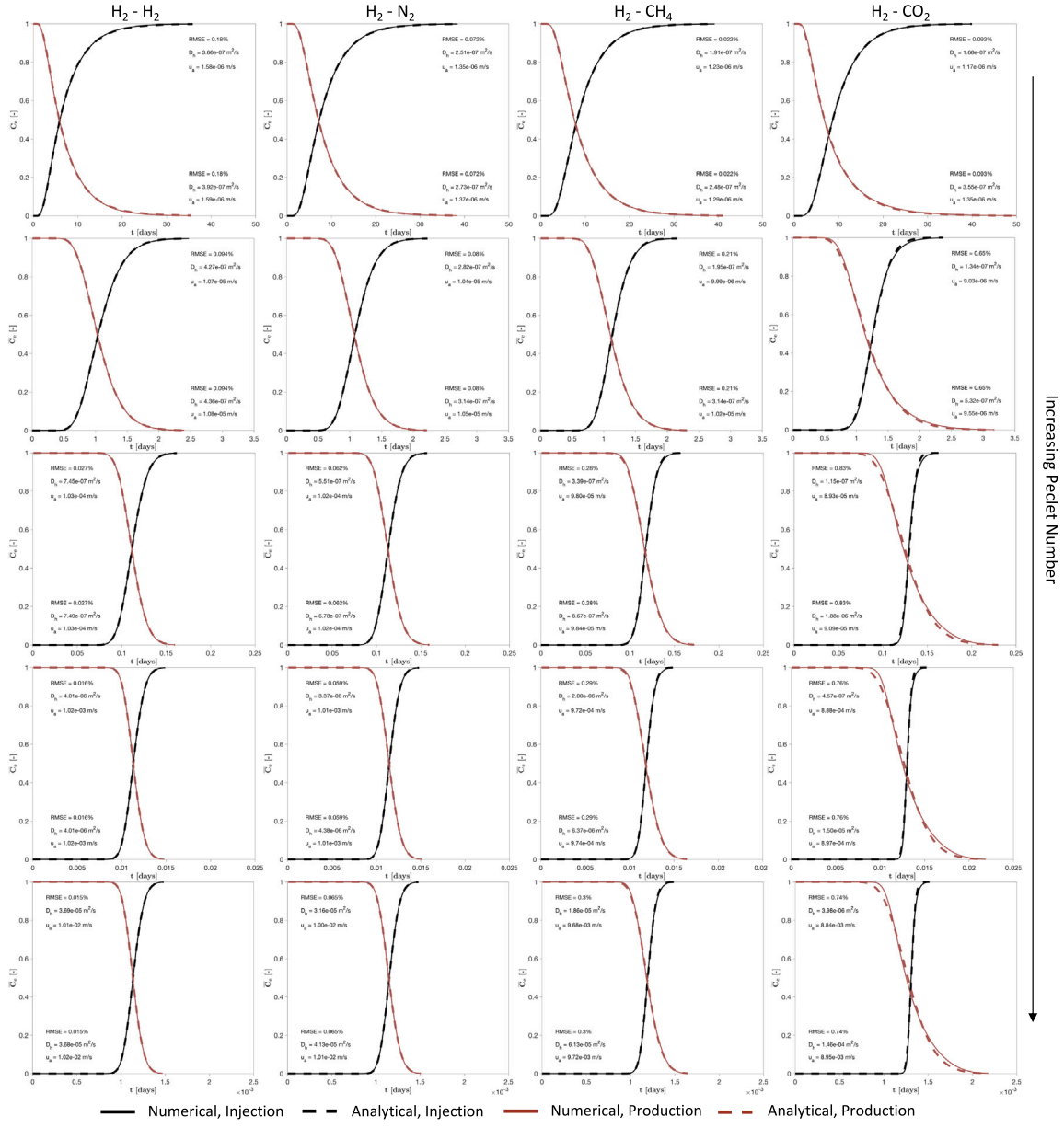

Fig. C.1. Simulated and fitted effluent concentrations versus time for different residing gases during injection and production of H_2. The effluent concentration data are fitted against the dispersion coefficient and velocity using the Ogata and Banks [49] analytical solution. u_a represents the fitted pore velocity based on the analytical solution.

of system components (hydrogen generator and MFCs).

- The increase in injection velocity was also ceased due to the low pore volume of the core plug.
- Despite the authors' best efforts to minimise tubing length (shown in red in Fig. B.1), it significantly contributed to gas mixing and dispersion due to its volume compared to the low pore volume of the core plug.
- The presence of the GC introduced further complications. Accurate concentration measurements required frequent and long sampling times. However, these experiments were limited in both regards. Frequent samplings and sampling times longer than one second were impractical due to the core plug's low pore volume. Additionally, GC sampling caused pressure fluctuations.
- Although the experiments were repeatable in each gas system, implementing identical boundary conditions for different gas systems was not possible due to (i) various pressure drops induced by the GC scans in different gas systems, (ii) different responses of the outlet MFC to resident gases, as it was calibrated only for the N_2 gas, and (iii) high compressibility of the gaseous systems.
- The current experimental setup also failed in terms of the reversed process direction, where the introduction of gases other than H_2 into an H_2 - filled system was not possible due to the backflow

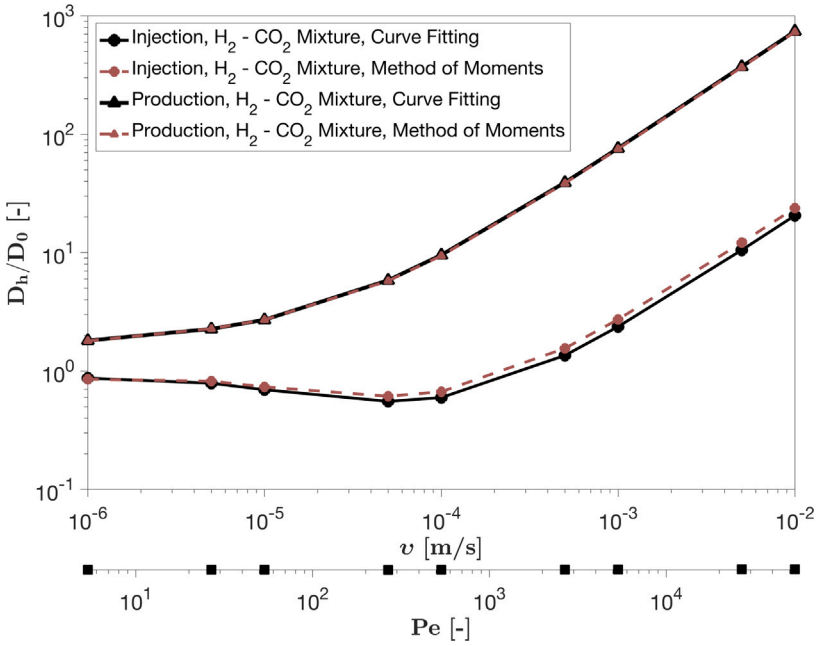

Fig. D.1. A comparison between the dispersion coefficients quantified by the method of moments [57] and computed based on curve fitting with the Ogata and Banks analytical solution [49].

of H_2. The reason behind such behaviour is not yet known to the authors.

For future experiments, modifications can be carried out to enable the setup of performing gas-mixing experiments at real-life conditions for hydrogen storage. These modifications include: (i) utilising core plugs with higher pore volumes, much larger than the volume of the connected tubing, and the amount of GC scans. This reduces the effect of tubing in the determination of correct dispersion coefficient, and the fluctuation caused by GC scans. Moreover, it provides the capability of performing experiments at higher Péclet numbers. (ii) Replacing MFCs and gas sources with the ones that withstand and operate at higher pressures (iii) Calibrating the outflow MFC for different gases.

Appendix C. Curve fitting results

Fig. C.1 presents the numerical and analytical effluent concentration data for the homogeneous simulation cases of this study at different Péclet numbers and for different combinations of gas mixtures. The numerical effluent data are fitted against average-domain dispersion coefficient and pore velocity using the Ogata and Banks [49] ADE analytical solution. The effluent is located at the right and left boundaries during injection and production, respectively. The fitted dispersion coefficients, pore velocities, and root mean square error (RMSE) for each case is shown in the corresponding plots.

Appendix D. Method of moments

Fig. D.1 compares the results of dispersion coefficients calculated based on the curve fitting of analytical solution [49] and the method of moments (based on step inputs) developed by Yu et al. [57]. The results show good agreement across all velocities, especially for the production cases.

Data availability

The data provided in this paper can be accessed at Nazari [71] in compliance with the CEJ's publishing policy.

References

[1] M.S. Costanza-Robinson, M.L. Brusseau, Gas phase advection and dispersion in unsaturated porous media, Water Resour. Res. 38 (2002) 7–1–7–9.
[2] M.S. Costanza-Robinson, M.L. Brusseau, Gas-phase dispersion in porous media, in: Gas Transport in Porous Media, Springer, 2006, pp. 121–132.
[3] S.W. Webb, Gas-Phase Diffusion in Porous Media: Evaluation of an Advective-Dispersive Formulation and the Dusty-Gas Model Including Comparison To Data for Binary Mixtures, Technical Report, Sandia National Lab.(SNL-NM), Albuquerque, NM (United States), 1996.
[4] C.K. Ho, S.W. Webb, Gas Transport in Porous Media, Volume 20, Springer, 2006.
[5] Y. Gong, M. Piri, Pore-to-core upscaling of solute transport under steady-state two-phase flow conditions using dynamic pore network modeling approach, Transp. Porous Media 135 (2020) 181–218.
[6] D. Li, C. Li, B. Gao, Y. Li, H. Sun, M. Wang, Transport of n-doped graphene in saturated porous media, Chem. Eng. J. 360 (2019) 24–29.
[7] L. Liu, B. Gao, L. Wu, V.L. Morales, L. Yang, Z. Zhou, H. Wang, Deposition and transport of graphene oxide in saturated and unsaturated porous media, Chem. Eng. J. 229 (2013) 444–449.
[8] Y. Chen, H. Steeb, H. Erfani, N.K. Karadimitriou, M.S. Walczak, M. Ruf, D. Lee, S. An, S. Hasan, T. Connolley, et al., Nonuniqueness of hydrodynamic dispersion revealed using fast 4d synchrotron x-ray imaging, Sci. Adv. 7 (2021) eabj0960.
[9] H. Erfani, N. Karadimitriou, A. Nissan, M.S. Walczak, S. An, B. Berkowitz, V. Niasar, Process-dependent solute transport in porous media, Transp. Porous Media 140 (2021) 421–435.
[10] A. Puyguiraud, P. Gouze, M. Dentz, Pore-scale mixing and the evolution of hydrodynamic dispersion in porous media, Phys. Rev. Lett. 126 (2021) 164501.
[11] M. Dentz, T. Le Borgne, A. Englert, B. Bijeljic, Mixing, spreading and reaction in heterogeneous media: A brief review, J. Contam. Hydrol. 120 (2011) 1–17.
[12] A. Saeibehrouzi, S. Abolfathi, P. Denissenko, R. Holtzman, Pore-scale modeling of solute transport in partially-saturated porous media, Earth-Sci. Rev. (2024a) 104870.
[13] A. Saeibehrouzi, R. Holtzman, P. Denissenko, S. Abolfathi, Solute transport in unsaturated porous media with spatially correlated disorder, Adv. Water Resour. (2024b) 104773.
[14] M. Bai, Z. Liu, J. Zhang, L. Lu, Prediction and experimental study of mass transfer properties of micronanobubbles, Ind. Eng. Chem. Res. 60 (2021) 8291–8300.
[15] Y. Guo, J. Lou, J.K. Cho, N. Tilton, J. Chun, W. Um, X. Yin, K.B. Neeves, N. Wu, Transport of colloidal particles in microscopic porous medium analogues with surface charge heterogeneity: Experiments and the fundamental role of single-bead deposition, Environ. Sci. Technol. 54 (2020) 13651–13660.
[16] J. Mathiesen, G. Linga, M. Misztal, F. Renard, T. Le Borgne, Dynamic fluid connectivity controls solute dispersion in multiphase porous media flow, Geophys. Res. Lett. 50 (2023) e2023GL105233.
[17] S. Kamrava, J. Im, F.P. de Barros, M. Sahimi, Estimating dispersion coefficient in flow through heterogeneous porous media by a deep convolutional neural network, Geophys. Res. Lett. 48 (2021) e2021GL094443.

[18] J. Zeng, J. Liu, J. Guo, Characterization of gas transport in shale: A multi-mechanism permeability modeling approach, Chem. Eng. J. 438 (2022) 135604.
[19] T.J. Hughes, A. Honari, B.F. Graham, A.S. Chauhan, M.L. Johns, E.F. May, Co2 sequestration for enhanced gas recovery: New measurements of supercritical co2–ch4 dispersion in porous media and a review of recent research, Int. J. Greenh. Gas Control. 9 (2012) 457–468.
[20] A. Honari, T.J. Hughes, E.O. Fridjonsson, M.L. Johns, E.F. May, Dispersion of supercritical co2 and ch4 in consolidated porous media for enhanced gas recovery simulations, Int. J. Greenh. Gas Control. 19 (2013) 234–242.
[21] C. Oldenburg, S. Benson, Carbon Sequestration with Enhanced Gas Recovery: Identifying Candidate Sites for Pilot Study, Technical Report, Lawrence Berkeley National Lab.(LBNL), Berkeley, CA (United States), 2001.
[22] C.M. Oldenburg, Carbon dioxide as cushion gas for natural gas storage, Energy & Fuels 17 (2003) 240–246.
[23] S. Hogeweg, J. Michelsen, B. Hagemann, L. Ganzer, Empirical and numerical modelling of gas–gas diffusion for binary hydrogen–methane systems at underground gas storage conditions, Transp. Porous Media 151 (2024) 213–232.
[24] K. Yang, S. Kobeissi, N. Ling, M. Li, L. Esteban, E.F. May, M.L. Johns, Measurement of hydrogen dispersion in rock cores using benchtop nmr, Int. J. Hydrog. Energy 48 (2023) 17251–17260.
[25] F. Nazari, R. Farajzadeh, V.J. Niasar, Critical parameters controlling wettability in hydrogen underground storage-an analytical study, JCIS Open 8 (2022) 100063.
[26] F. Nazari, S.A. Nafchi, E.V. Asbaghi, R. Farajzadeh, V.J. Niasar, Impact of capillary pressure hysteresis and injection-withdrawal schemes on performance of underground hydrogen storage, Int. J. Hydrog. Energy 50 (2024) 1263–1280.
[27] S. Omrani, M. Ghasemi, M. Singh, S. Mahmoodpour, T. Zhou, M. Babaei, V. Niasar, Interfacial tension–temperature–pressure–salinity relationship for the hydrogen–brine system under reservoir conditions: integration of molecular dynamics and machine learning, Langmuir 39 (2023) 12680–12691.
[28] C.S. Tan, D.C. Liou, Axial dispersion of supercritical carbon dioxide in packed beds, Ind. Eng. Chem. Res. 28 (1989) 1246–1250.
[29] S. Kobeissi, N.N. Ling, K. Yang, E.F. May, M.L. Johns, Dispersion of hydrogen in different potential cushion gases, Int. J. Hydrog. Energy 60 (2024) 940–948.
[30] E.M. Thaysen, A. Hassanpouryouzband, K. Edlmann, Hydrogen reservoir flow behaviour: Measurements of molecular diffusion, mechanical dispersion and relative permeability, 2023.
[31] K. Dabrowski, Laboratory determination of hydrogen/methane dispersion in rock cores for underground hydrogen storage, Energy Rep. 11 (2024) 4290–4296.
[32] A.M. Tartakovsky, D.M. Tartakovsky, P. Meakin, Stochastic langevin model for flow and transport in porous media, Phys. Rev. Lett. 101 (2008) 044502.
[33] Z. Chen, Reservoir Simulation: Mathematical Techniques in Oil Recovery, SIAM, 2007.
[34] H. Darcy, The Public Fountains of the City of Dijon, Victor Dalmont, Paris, France, 1856.
[35] A. Fick, V. on liquid diffusion, Lond. Edinb. Dublin Philos. Mag. J. Sci. 10 (1855) 30–39.
[36] R. Krishna, J.A. Wesselingh, The maxwell-stefan approach to mass transfer, Chem. Eng. Sci. 52 (1997) 861–911.
[37] D. Bothe, On the maxwell-stefan approach to multicomponent diffusion, Parabol. Probl.: Herbert Amann Festschr. (2011) 81–93.
[38] B. Tjaden, S.J. Cooper, D.J. Brett, D. Kramer, P.R. Shearing, On the origin and application of the bruggeman correlation for analysing transport phenomena in electrochemical systems, Curr. Opin. Chem. Eng. 12 (2016) 44–51.
[39] Z. Liu, H. Emami-Meybodi, Apparent diffusion coefficient for adsorption-controlled gas transport in nanoporous media, Chem. Eng. J. 450 (2022) 138105.
[40] B.E. Poling, The properties of gases and liquids, 2004.
[41] C. Wilke, C. Lee, Estimation of diffusion coefficients for gases and vapors, Ind. Eng. Chem. 47 (1955) 1253–1257.
[42] M.R. Riazi, C.H. Whitson, Estimating diffusion coefficients of dense fluids, Ind. Eng. Chem. Res. 32 (1993) 3081–3088.
[43] D.-Y. Peng, D.B. Robinson, A new two-constant equation of state, Ind. Eng. Chem. Fundam. 15 (1976) 59–64.
[44] J. Gross, G. Sadowski, Application of the perturbed-chain saft equation of state to associating systems, Ind. Eng. Chem. Res. 41 (2002) 5510–5515.
[45] O. Kunz, R. Klimeck, W. Wagner, M. Jaeschke, The gerg-2004 wide-range equation of state for natural gases and other mixtures, 2007.
[46] O. Kunz, W. Wagner, The gerg-2008 wide-range equation of state for natural gases and other mixtures: an expansion of gerg-2004, J. Chem. Eng. Data 57 (2012) 3032–3091.
[47] T.H. Chung, M. Ajlan, L.L. Lee, K.E. Starling, Generalized multiparameter correlation for nonpolar and polar fluid transport properties, Ind. Eng. Chem. Res. 27 (1988) 671–679.
[48] C.R. Wilke, A viscosity equation for gas mixtures, J. Chem. Phys. 18 (1950) 517–519.
[49] A. Ogata, R.B. Banks, A Solution of the Differential Equation of Longitudinal Dispersion in Porous Media, US Government Printing Office, 1961.
[50] P. Grathwohl, Diffusion in Natural Porous Media: Contaminant Transport, Sorption/Desorption and Dissolution Kinetics, Volume 1, Springer Science & Business Media, 2012.
[51] P. De Anna, T. Le Borgne, M. Dentz, A.M. Tartakovsky, D. Bolster, P. Davy, Flow intermittency, dispersion, and correlated continuous time random walks in porous media, Phys. Rev. Lett. 110 (2013) 184502.
[52] Y. Liang, B. Wen, M.A. Hesse, D. DiCarlo, Effect of dispersion on solutal convection in porous media, Geophys. Res. Lett. 45 (2018) 9690–9698.
[53] S. Omrani, C. Green, M. Sahimi, V. Niasar, Anomalies of solute transport in flow of shear-thinning fluids in heterogeneous porous media, Phys. Fluids 36 (2024).
[54] M. Dentz, T. Le Borgne, D. Lester, F.P. de Barros, Mixing in porous media, 2016.
[55] M.L. Verlaan, Dispersion in heterogeneous media: Fundamental issues inspired by underground gas storage, 2001.
[56] M.L. Verlaan, C. van Kruijsdijk, The effect of connate water on gas mixing in porous media-non-equilibrium mass transfer, in: ECMOR VI-6th European Conference on the Mathematics of Oil Recovery, European Association of Geoscientists & Engineers, 1998, pp. cp–102.
[57] C. Yu, A. Warrick, M. Conklin, A moment method for analyzing breakthrough curves of step inputs, Water Resour. Res. 35 (1999) 3567–3572.
[58] M. Dentz, J.J. Hidalgo, D. Lester, Mixing in porous media: concepts and approaches across scales, Transp. Porous Media 146 (2023) 5–53.
[59] A. D'Onofrio, V. Freytes, M. Rosen, C. Allain, J. Hulin, Echo tracer dispersion in flows of polymer solutions through porous media: A tool for detecting weak permeability heterogeneities? Eur. Phys. J. E 7 (2002) 251–259.
[60] J. Hulin, T. Plona, Echotracer dispersion in porous media, Phys. Fluids A: Fluid Dyn. 1 (1989) 1341–1347.
[61] D.G. Dronfield, S.E. Silliman, Velocity dependence of dispersion for transport through a single fracture of variable roughness, Water Resour. Res. 29 (1993) 3477–3483.
[62] A. Hassanpouryouzband, E. Joonaki, K. Edlmann, N. Heinemann, J. Yang, Thermodynamic and transport properties of hydrogen containing streams, Sci. Data 7 (2020) 222.
[63] A.W. Ameen, J. Ji, M. Tamaddondar, S. Moshenpour, A.B. Foster, X. Fan, P.M. Budd, D. Mattia, P. Gorgojo, 2D boron nitride nanosheets in pim-1 membranes for co2/ch4 separation, J. Membr. Sci. 636 (2021) 119527.
[64] M. Yu, A.B. Foster, M. Alshurafa, J.M. Luque-Alled, P. Gorgojo, S.E. Kentish, C.A. Scholes, P.M. Budd, Co2 separation using thin film composite membranes of acid-hydrolyzed pim-1, J. Membr. Sci. 679 (2023) 121697.
[65] Agilent, Gas chromatography fundamentals.
[66] L. Klinkenberg, The permeability of porous media to liquids and gases, Drill. Prod. Pr. (2012) 200–213, URL: https://api.semanticscholar.org/CorpusID:54042399.
[67] R. Aris, On the dispersion of a solute in a fluid flowing through a tube, Proc. R. Soc. Lond. Ser. A. Math. Phys. Sci. 235 (1956) 67–77.
[68] V. Chandra, S. Das, E. Peters, J. Kuipers, Direct numerical simulation of hydrodynamic dispersion in open-cell solid foams, Chem. Eng. J. 358 (2019) 1305–1323.
[69] J. Yang, P. Zhang, A concise pore structure model for predicting the effective ion diffusion coefficients of cementitious materials, Constr. Build. Mater. 265 (2020) 120321.
[70] M.T.Q.S. da Silva, M. do Rocio Cardoso, C.M.P. Veronese, W. Mazer, Tortuosity: A brief review, Mater. Today: Proc. 58 (2022) 1344–1349.
[71] F. Nazari, Implications of non-ideal gas dispersion for underground hydrogen storage, 2024, http://dx.doi.org/10.17632/xvv5v7gznj.3.